Advanced Pyroelectric Materials for High-Performance Infrared Detection: Design, Simulation, and Optimization using Finite Element Method in COMSOL Multiphysics

Meenakshi Rajpurohit*[a] , Rahul Sinha[b] , Pankaj B Agarwal[c], Rajesh Purohit[d] and Anurag Namdev[e]

[a] *MTech, Department of Physics, MANIT, Bhopal, MP, India.*
[b] *PhD, Department of Chemical Engineering Indian Institute of Technology Tirupati, AP, India.*
[c] *Senior Principal Scientist, CSIR-CEERI, Pilani, Rajasthan, India.*
[d] *Professor, Mechanical Engineering Department, MANIT, Bhopal, MP, India.*
[e] *Assistant Professor, Mechanical Engineering Department, Institute of Engineering and Technology, Lucknow (UP), India.*

E mail: meenakshirajpurohit13@gmail.com, pankaj@ceeri.res.in, ch21d503@iittp.ac.in, rpurohit73@gmail.com; anumech10@gmail.com
**Corresponding Author Email: meenakshirajpurohit13@gmail.com*

Abstract

Pyroelectric materials have attracted significant attention due to their unique properties, such as natural polarization, high sensitivity, fast response, and low power consumption. These materials are widely used in developing high-performance infrared (IR) detectors for various applications, including fire alarms, gas sensors, night vision, pollution monitoring, thermal imaging, medical imaging, and surveillance. One of the most promising pyroelectric materials for IR detector applications is lithium tantalate ($LiTaO_3$). $LiTaO_3$ possesses exceptional material properties, such as a high pyroelectric coefficient, low thermal conductivity, and low temperature dependence, making it an excellent choice for high-performance pyroelectric radiation detectors. Additionally, the utilization of ultra-thin films of $LiTaO_3$ can enhance the detector's performance by increasing the absorption of incoming radiation and improving the mechanical stiffness of the device. One approach is to use a cavity geometry at the bottom of the device, which can increase the mechanical strength and radiation absorption of the detector. The pyroelectric infrared (IR) detector is constructed with several layers, each serving specific functions. At the bottom lies a silicon substrate, acting as the foundation of the detector. Above it, a SiO_2 cavity structure acts as a thermal isolation layer. On top of the SiO_2 layer, a Molybdenum layer functions as the bottom electrode. Sandwiched between the Molybdenum and Titanium Nitride (TiN) electrodes is the AIN sensing layer, the crucial component responsible for detecting IR radiation. The top electrodes, comprising a TiN top electrode and an aluminum electrode, facilitate contact surfaces for the detector. The top absorber stack consists of three layers: SiO_2, SiN, and SiO_2. This stack is carefully designed to maximize the absorption of incident thermal radiation through destructive interference between incident and reflected waves in the dielectric absorber stack. As the incident IR radiation interacts with the pyroelectric material, it generates thermal energy that leads to a change in polarization, producing an electrical output signal. To increase mechanical stiffness and ensure support for the absorber stack, a SiO_2 rib array structure is designed underneath the bottom Molybdenum electrode. The rectangular sensing and structural layers, made of materials such as $LiTaO_3$, $LiNbO_3$, and AlN, are finely meshed for better accuracy and simulation speed. Finite Element Method (FEM) simulation has been widely used for designing, modeling, and simulating pyroelectric-based IR detectors.

Keywords: *Infrared sensors; Microelectromechanical systems (MEMS); Pyroelectric devices; Pyroelectric Materials; Heat transfer in solids; electrostatics.*

1. Introduction

In the realm of infrared detection, two primary categories emerge: Uncooled IR detectors, often referred to as thermal detectors, and cooled IR detectors, recognized as photon detectors. Within the uncooled domain, we find Pyroelectric, Bolometers, and Thermopile technologies, while in the cooled sphere, Photovoltaic, Photoconductive, and Photodiode technologies take precedence [1-6]. Pyroelectric materials, employed in the development of infrared (IR) detectors, typically function at room temperature. These materials belong to the subset of piezoelectric materials, and within this category, ferroelectric materials can be further classified as a subset of pyroelectric materials. Pyroelectric materials exhibit a distinctive inherent polar axis even in the absence of external strains. This inherent characteristic suggests that pyroelectric crystals are inherently polarized within specific temperature ranges. When subjected to an electric field, the spontaneous polarization of these crystals can be feasibly reoriented. The lithium niobate pyroelectric material has extraordinary pyroelectric property used to make CMOS compatible infra-red (IR) sensors [7–11] and suitable for mass production. The temperature sensitivity is maximum and thermal time constant is optimum in the case of lithium niobate based infra-red sensors. Aluminum nitride (AlN)[12] is a III-V compound with a hexagonal wurtzite crystal structure that has gained increasing interest for piezoelectric and photoelectric applications. AlN has a high decomposition temperature and low electrical, but high thermal conductivity making it an ideal candidate for use in high temperature applications and in harsh environments. Crystalline lithium tantalate ($LiTaO_3$)[13] is well known for its unique optical and ferroelectric properties, the physical basics states that the performance of pyroelectric radiation detectors increases with reduction of sensor element film thickness. Consequently, ultrathin pyroelectric films are targeted to improve detector performance. Thereby, $LiTaO_3$ bulk material has become the first-choice sensor material for high-performance pyroelectric radiation detectors because of its excellent sensor-specific material properties and the very low temperature influence on the sensor parameters.[14]–[16] FEM provides integrated environment for application design and physics simulation. Pyroelectric based infrared detectors have several advantages like pyroelectric detectors have wider spectral bandwidth, sensitivity within broad temperature range, less power consumption, fast response time, low-cost construction[17]–[19]. In this paper three Pyroelectric materials ($LaTiO_3$, $LiNbO_3$ and AlN) sensing layer for infra-red detector has been designed and Simulation is performed. It's been reported that $LaTiO_3$ based infrared detector has obtained maximum current across aluminum electrodes hence better responsivity than $LiNbO_3$ and AlN based IR detector. To improve the performance of $LiTaO_3$-based IR detectors, researchers have focused on optimizing the device design and fabrication process.

2. Design Considerations

An infrared (IR) sensor based on CMOS-compatible aluminum nitride (AlN) pyroelectric material has been meticulously designed to enhance multiple aspects of its performance. This includes amplifying the output electrical signal, bolstering mechanical rigidity, and optimizing the absorption of IR radiation. The structural arrangement, illustrated in Figure 1, showcases the configuration of the pyroelectric IR detector. The core of this design entails a pyroelectric AlN layer, strategically positioned as the sensing layer. This layer is seamlessly situated between two key components: the upper electrode composed of titanium nitride (TiN) and the lower electrode constructed from molybdenum (Mo). Notably, the TiN layers, characterized by their remarkably thin nature (approximately 30 nm in thickness), are purposefully engineered to not function as thermal barriers. Their thinness ensures that they do not impede the thermal transfer within the device. In this context, the aluminum layer plays a pivotal role by serving as the primary contact surface, facilitating an efficient and reliable electrical connection. This meticulously engineered layer arrangement collectively bestows upon the sensor an array of advantageous attributes. These include an elevated level of sensitivity, bolstered mechanical stability, and a finely tuned capability to optimize the absorption of energy, specifically aimed at infrared (IR) detection objectives. Furthermore, the uppermost segment of the sensor comprises an absorber stack composed of distinct layers: silicon dioxide (SiO_2), silicon nitride (SiN), and another layer of silicon dioxide (SiO_2), sequentially arranged. This absorber stack plays a pivotal role in the sensor's overall performance by aiming to maximize the absorption of incident thermal radiation, particularly within the infrared spectrum. This intricate configuration effectively enhances the sensor's capacity to capture and convert IR energy

into detectable electrical signals. The pyroelectric aluminum nitride (AlN) sensing layer plays a crucial role in receiving and absorbing the entirety of the thermal energy conveyed through the absorber stack. The mechanism for achieving this absorption hinges upon the concept of destructive interference between the incident and reflected waves within the dielectric absorber stack. This phenomenon is effectively orchestrated to maximize the absorption of energy. Within this context, the AlN thin layers, with a thickness of approximately 100 nanometers, have been observed to exhibit a remarkable transmission rate exceeding 90%, coupled with a reflective rate of less than 10%, over a wavelength span ranging from 1 to 3 micrometers. This optical behavior contributes to their capacity for effective energy absorption. The incident infrared (IR) radiation serves as the catalyst for generating thermal energy within the material. This energy influx prompts a modification in the polarization of the pyroelectric substance, thereby engendering an electrical output signal. To attain an optimal temperature sensing environment, the architecture of the sensor is meticulously designed to ensure thermal isolation. This is achieved through the incorporation of a thin membrane structure in the detector stack. Remarkably, the backside silicon (Si) substrate has been intentionally removed, further enhancing the sensor's ability to isolate and accurately sense temperature variations. While the fabrication of these kinds of structures is challenging and often results in membrane breakage, hence a decrease in the yield of the detector. To reduce membrane breakage a SiO_2 rib array[20] is designed for mechanical support. This SiO_2 ribs array structure is underneath the bottom MO electrode (Figure 1). This kind of design increases the mechanical stiffness of the membrane and ensures mechanical support for the absorber stack. Doris K. T. Ng et al. jointly reported a review letter which uses aluminum nitride pyroelectric material for infrared detection. For the deposition and polishing of the sensing layer, they utilized low pressure chemical vapour deposition tetraethyl orthosilicate (LPCVD TEOS)[21], deep reactive ion etching (DRIE) and chemical mechanical polishing (CMP)[22]. V. Norkus et al. published a review in which they explain how to use a patterned responsive element to increment responsivity of IR detector utilizes by lateral heat flux that increase the output signal[23-24]. M. Schossig and colleagues published a review in which single wafer of lithium tantalate pyroelectric material was fabricated utilizing ion ball milling procedures with a thickness about 0.4μm. Lithium tantalate wafer thickness is reduced down to 20μm, extremely thin gold electrode is applied on both side of the chip to from sensitive layer. for lowering the damage of the crystal chemical mechanical polishing is used. The IR detector consists of several structural layers, each with its own size and shape. The silicon substrate forms the foundation of the detector and has dimensions of 50 um in width, 1500 um in length, and 500 um in thickness. On top of the substrate, there is a SiO_2 cavity structure measuring 1500 um in width, 1500 um in length, and 0.425 um in thickness. A layer of molybdenum is present, which has a size of 1000 um in width, 1000 um in length, and 0.084 um in thickness. This layer serves as an important component for conductivity and electrical connections within the detector. The AIN sensing layer is responsible for capturing infrared radiation, and it measures 515 um in width, 515 um in length, and 0.169 um in thickness. This layer's size and shape are specifically designed to enhance sensitivity to infrared light. The TiN top electrode is another crucial layer, with dimensions of 1000 um in width, 1000 um in length, and 0.03 um in thickness. It serves as an electrode for the detector, facilitating the collection and transmission of electrical signals. Additionally, there is an aluminum electrode that measures 200 um in width, 550 um in length, and 1 um in thickness. This electrode plays a role in the electrical conductivity and connection within the detector. Lastly, the absorber stack, comprising layers of SiO_2/SiN/SiO_2, contributes to the absorption of infrared radiation. The SiO_2 layer has a thickness of 0.246 um, followed by the SiN layer with a thickness of 0.128 um, and another SiO_2 layer with a thickness of 0.290 um. These layers are designed to optimize the absorption of infrared light within the detector. The IR detector's structural layers have specific sizes and shapes tailored to enhance sensitivity, electrical conductivity, and absorption of infrared radiation. Each layer plays a crucial role in the functionality and performance of the detector for infrared light detection applications.

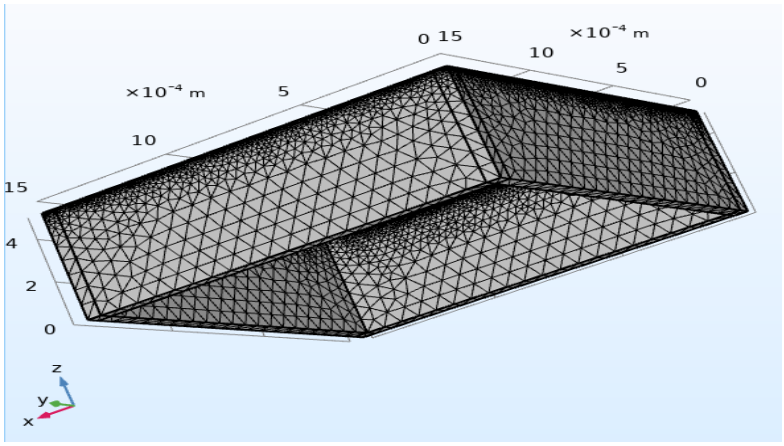

Figure 1: Diagram of pyroelectric IR detector showing all the structure layers.

3. Simulation

Simulation of an IR (Infrared) detector sensing layer with heat transfer in solids and electrostatics module involves analyzing the behavior of the detector under various conditions. It combines the principles of heat transfer in solids and electrostatics to understand how the IR sensing layer responds to thermal effects and electric fields. The heat transfer module is used to study the temperature distribution and heat flow within the IR detector sensing layer. It takes into account parameters such as material properties, thermal conductivity, and heat generation within the material. By simulating heat transfer we understood how temperature variations affect the performance of the IR detector and optimize its design. The electrostatics module focuses on analyzing the electric field distribution and potential within the IR detector sensing layer. It considers the properties of the material, such as its dielectric constant and conductivity, as well as the applied voltage or electric potential. By studying electrostatics, we evaluated the impact of electric fields on the performance and sensitivity of the IR detector. This simulation enables the investigation of the interplay between temperature variations, electric fields, and the resulting changes in the detector's response. By studying these factors, we optimized the design, enhanced the sensitivity, and improved the overall performance of the IR detector.

3.1 *Analytical input function*

Pyroelectric-based IR detectors rely on the detection of modulated radiation, where charges accumulate on the surfaces of the detector due to the orientation of dipole movements. The change in charge is then detected, highlighting the importance of using a chopper-like radiation that switches between ON and OFF states. This modulation is necessary to effectively capture the effect generated by the absorption of thermal radiation, making it an essential characteristic of pyroelectric sensors. In the COMSOL Multiphysics simulation for the IR detector, a rectangular wave function shown in figure (2) named "an1" was employed to provide the desired chopper-like input. The function was defined as "rect1(t)" with respect to time and designed to mimic the periodic switching pattern of the radiation. Specifically, the rectangular wave function was configured to have a lower limit of 0 and an upper limit of 8, ensuring the periodic nature of the ON-OFF modulation required for effective detection of thermal radiation effects.

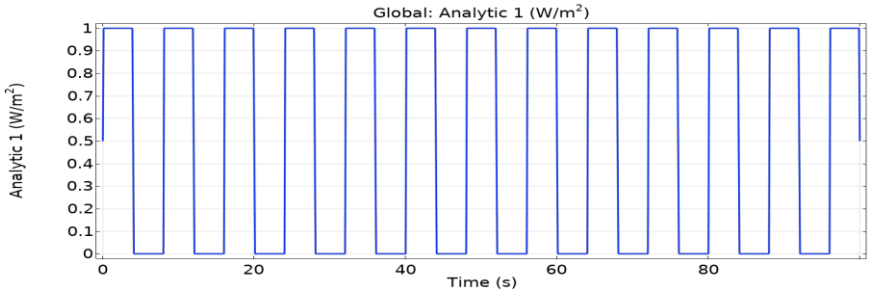

Figure 2: The input power in a rectangular waveform is represented as a function of time, exhibiting a periodic pattern

3.2 Size, shape and position of pyroelectric sensing layer

The sensing layer in the infrared (IR) detector has a specific shape and size, measuring 3 mm x 3 mm x 0.03 mm. However, the thickness of the sensing layer is considered to be too small. In order to address this issue, the thin sensing layer made of aluminium nitride (AlN) was replaced with lithium niobate ($LiNbO_3$) and lithium tantalate ($LiTaO_3$) pyroelectric materials [25]. Comparative analysis was conducted to observe the performance differences between these materials. To accurately model and simulate the behavior of the sensing layer, relevant material properties such as heat capacity, thermal conductivity, coefficient of thermal expansion, and isotropic tangent coefficient of thermal expansion were assigned in the Finite Element Method (FEM) simulation. These material properties play a crucial role in determining the thermal response and behavior of the sensing layer within the IR detector. The pyroelectric layer within the system is characterized by specific dimensions. The length, breadth, and height of the pyroelectric layer are denoted by lp, bp, and tp, respectively, and have values of 3 mm, 3 mm, and 0.03 mm. In the system, lp represents the length of the pyroelectric layer, bp represents the breadth, and tp represents the height shown in figure 3, These dimensions are crucial parameters that determine the geometric characteristics and overall structure of the pyroelectric layer.

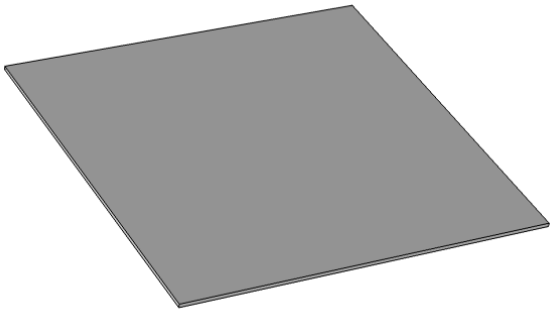

Figure 3: Design of rectangle shaped sensing layer of pyroelectric IR detector

3.3 Pyroelectric Material's property and value used

In COMSOL software, the three pyroelectric materials used as the sensing layer in the IR detector are Aluminium Nitride, Lithium Tantalate, and Lithium Niobate. The following properties have been assigned specific values for each material is shown in Table (1).

Table 1. Values of pyroelectric material properties used for sensing layer

Material Property	Lithium Tantalate	Lithium Niobate	Aluminum Nitride
Relative Permittivity	{40.9, 40.9, 43.3}	{43.6,43.6,29.16}	9
Density	7450 kg/m^3	4700 kg/m^3	3300 kg/m^3
Thermal Conductivity	4.6W/(m·K)	4.2W/(m·K)	321W/(m·K)
Heat capacity at constant pressure	600 J/(kg·K)	628 J/(kg·K)	800 J/(kg·K)
Total pyroelectric coefficient	{0,0, -176e-6}C/(m²·K)	{0,0, -8.3e-5}C/(m²·K)	{0, 0, -7e-6}C/(m²·K)

3.4 Heat Transfer in solid

We have analyzed the heat transfer in a solid material, and also considered the role of heat loss on the edges, top, and bottom surfaces of the pyroelectric sensing layer. These surfaces play a significant role in determining the overall heat distribution within the AlN, $LiTaO_3$ and $LiNbO_3$. The edges of

the pyroelectric sensing layer can act as heat sinks or sources, depending on the boundary conditions and the surrounding environment. Heat loss from the edges occurs through conduction, convection, and radiation. If the edges are in contact with a cooler medium, heat is transferred from the sensing layer to the surroundings, resulting in a temperature decrease in the material. Conversely, if the edges are exposed to a warmer environment, the heat will be transferred into the sensing layer, leading to a temperature increase. The top surface of the pyroelectric sensing layer is typically exposed to the surroundings and can experience heat loss through various mechanisms. Convection and radiation are the primary modes of heat transfer from the top surface. Convection involves the transfer of heat through the movement of air or fluid in contact with the surface, while radiation refers to the emission of thermal energy in the form of electromagnetic waves. The rate of heat loss from the top surface depends on factors such as the temperature gradient, surface area, and properties of the surrounding medium. Similarly, the bottom surface of the pyroelectric sensing layer can also contribute to heat loss. Depending on the setup, the bottom surface may be in contact with a substrate, heat sink, or another medium. Heat transfer from the bottom surface occurs through conduction and, depending on the conditions, also through convection or radiation. The nature of the boundary conditions and the thermal properties of the materials involved will determine the magnitude of heat loss from the bottom surface.

3.4.1 Heat loss from edges

A wall height of 0.03 mm was selected to represent the edges of the sensing layer. The heat loss from these edges was considered using a convective heat flux as the chosen flux type. In order to simulate the heat transfer accurately, it is important to define the geometry and dimensions of the solid model within the software. For the edges, a wall height of 0.03mm was specified to represent their thickness. To incorporate heat loss from the edges, a convective heat flux boundary condition was applied. This boundary condition accounts for the transfer of heat through convection, which is the process of heat exchange between a solid surface and the surrounding fluid medium. The convective heat flux accounts for the heat transfer rate based on factors such as the temperature difference between the solid surface and the fluid, the thermal properties of the fluid, and the convective heat transfer coefficient.

3.4.2 Heat loss from top surface

When studying heat transfer in solids using COMSOL software, the heat loss from the top surface was considered. The characteristic length (L) shown in eq. (1) was determined using the eq. (2), where lp represents the length of the pyroelectric sensing layer and bp denotes its width. For the top surface, a thickness of 0.03mm (tp) was considered, while the length (lp) was taken as 3mm. By incorporating these parameters, the software accurately accounted for heat loss from the top surface, allowing for a comprehensive analysis of heat transfer dynamics in the solid material. This information facilitates the optimization and design of heat transfer processes in various applications.

$$Characteristic\ length\ (L) = \frac{area}{perimeter} \quad eq.(1)$$

$$\mathrm{L\,(m)} = (\mathrm{lp} * \mathrm{bp}) / ((2 * \mathrm{lp}) + (2 * \mathrm{bp})) \quad \mathrm{eq.(2)}$$

3.4.3 Heat loss from bottom

In the study of heat transfer in solids using COMSOL software, the heat loss from the bottom surface was taken into account. The characteristic length (L) was determined using the eq. (2), where lp represents the length of the pyroelectric sensing layer and bp denotes its width. The bottom surface was subjected to a convective heat flux boundary condition, considering the transfer of heat through convection. This boundary condition considers factors such as the temperature difference, fluid properties, and convective heat transfer coefficient. By incorporating these parameters, COMSOL software accurately models heat loss from the bottom surface, enabling a comprehensive analysis of heat transfer dynamics in the solid material.

3.4.4 Deposited beam power

Deposited beam power refers to the power delivered by a beam, such as a laser or electron beam, onto the surface of a solid material. The deposited beam power given in eq. (3) plays a significant role in understanding the heat transfer dynamics and thermal response of the material. We specified the characteristics of the beam, including its power density distribution and spatial profile. These

parameters can be adjusted based on experimental data or theoretical models. It enables the study of temperature distribution, thermal gradients, and thermal response based on the power distribution of the incident beam. Heat transfer in solids modules also allow for the specification of the beam orientation. The beam orientation refers to the direction in which the beam propagates or irradiates the solid material. We considered the exponential decay factor along the x, y, and z directions. In the case of an exponential decay factor of 0, 0, 1 in the x, y, and z directions respectively, it indicates that the beam propagates predominantly in the z-direction, perpendicular to the surface of the material. an1(t) is analytic input function shown in figure 2.

$$beam\ power\ density\ (Io) = 500 * an1(t)\ \frac{W}{m^2} \qquad eq.(3)$$

3.5 *Electrostatics (es) study*

The electrostatic module analysed and simulated the behaviour of electric fields and charges in the pyroelectric sensing layer of infrared (IR) detectors. A pyroelectric sensing layer is a key component that converts incident IR radiation into electrical signals. The electrostatic module allows for the investigation of the electric field distribution within the pyroelectric material, aiding in the optimization of its performance. This module enables the calculation of key parameters such as electric potential and electric field strength. In the electric circuit part of electrostatics study, specific components such as capacitors and resistors can be included to model the behavior of the system. For instance, in the context of analyzing pyroelectric sensing layers in IR detectors, a capacitor with a value of 100 nF and a resistor with a value of 1000 Ω can be utilized. The capacitor, with a capacitance of 100 nF, represents the ability of the pyroelectric sensing layer to store electrical charge. It captures the charge generated by the pyroelectric effect in response to incident IR radiation. The value of 100 nF determines the capacitance of the capacitor and influences the overall electrical response of the system. Additionally, the resistor with a value of 1000 Ω is employed to model the electrical resistance within the circuit. It represents the load or external circuit connected to the pyroelectric sensing layer. The resistor value of 1000 Ω determines the level of electrical resistance and influences the behavior of the electrical signals generated by the pyroelectric sensing layer. By incorporating these specific values for the capacitor and resistor within the electric circuit part of COMSOL software, accurate simulations can be performed to analyze the electrical response of the pyroelectric sensing layer in IR detectors. This allows for the optimization and design of efficient and reliable IR detection systems.

3.6 *Multiphysics*

We performed a simulation of Multiphysics phenomena by coupling the electrostatics and heat transfer of solid modules within the pyroelectricity module in COMSOL software. By utilizing the pyroelectricity module, we were able to simultaneously analyse the electrical and thermal behaviour of the pyroelectric material. This module allowed for the incorporation of both the electrostatics module, which accounted for electric field distribution and charge accumulation within the material, and the heat transfer of the solid module, which considered temperature distribution and thermal response. The coupling of these modules enabled a comprehensive investigation of the Multiphysics interactions occurring in the pyroelectric material. It allowed us to understand the coupled effects between electrical charge generation, distribution, and thermal changes within the material due to incident infrared radiation. Through this simulation approach, we were able to gain insights into the pyroelectric response, including the electrical potential distribution, charge accumulation, and temperature changes in the material. This information facilitated a deeper understanding of the pyroelectric properties and the optimization of pyroelectric-based devices such as infrared detectors.

3.7 *Meshing*

The physics control meshing of the pyroelectric sensing layer in an IR detector is a critical step in the simulation process within COMSOL software. It involves defining the meshing parameters that govern the discretization of the pyroelectric material, determining the resolution and accuracy of the simulation. Meshing refers to the division of the geometry into smaller elements or cells, which form the basis for numerical calculations in COMSOL. In the case of the pyroelectric sensing layer, a high-quality mesh with appropriate element sizes and distribution is essential to capture the complex phenomena occurring within the material. The significance of physics control meshing lies in its impact on the accuracy, computational efficiency, and convergence of the simulation. A properly meshed pyroelectric sensing layer ensures that the numerical solution is robust and reliable. It allows for capturing intricate features, such as thin regions or gradients in the material, accurately representing the physics at play. By refining the mesh in regions of interest or near boundaries, the physics control meshing enables the simulation to accurately capture variations in electric fields, charge distribution, temperature gradients, and other relevant quantities within the pyroelectric sensing layer. This level of detail and accuracy is crucial for obtaining realistic and meaningful results. Moreover, an optimal meshing strategy helps in balancing computational resources and simulation time. By appropriately defining mesh parameters, such as element size and density, the computational burden can be minimized without compromising the accuracy of the results. In summary, the physics control meshing shown in figure (4) of the pyroelectric sensing layer in an IR detector within COMSOL software plays a significant role in achieving accurate and efficient simulations. It ensures the capture of intricate physics, such as electric field distribution and temperature gradients, while optimizing computational resources. Proper meshing enhances the reliability and realism of the simulation, enabling researchers and engineers to gain valuable insights into the performance and behaviour of pyroelectric-based IR detectors.

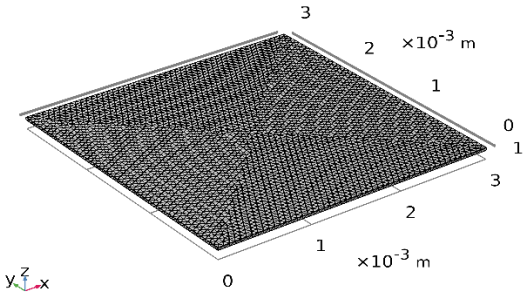

Figure 4: Physics controlled Meshing of sensing layer

4. Results and discussion

4.1 Thermal analysis of sensing layer

a. Temperature distribution

In the results section of the pyroelectric sensing layer in COMSOL software, the temperature distribution curve, measured in Kelvin, reveals important insights into the thermal behaviour of the materials. The curve shown in figure (5) represents how the temperature varies across different locations within the sensing layer. Upon analysing the temperature distribution curve, it becomes evident that the corners of the sensing layer exhibit lower temperatures compared to the middle region. This observation suggests that heat dissipation is relatively higher at the corners, resulting in lower temperatures in those areas. On the other hand, the middle of the sensing layer exhibits a higher temperature distribution, exceeding 302 Kelvin (K). This signifies that heat accumulates or is trapped more in the central region, leading to increased temperatures. The temperature distribution curve provides valuable information about the thermal characteristics of the pyroelectric sensing layer. It helps identify areas of potential temperature variations, which can impact the overall performance

and sensitivity of the IR detector. By understanding the temperature distribution, researchers and engineers can optimize the design and placement of heat sinks, insulation materials, or other cooling mechanisms to mitigate temperature variations and enhance the performance of the pyroelectric sensing layer. After simulating the temperature distribution of $LiTaO_3$(top right), $LiNbO_3$ (top left) and AlN (bottom) sensing layer it can be observed that AlN heats slightly faster then $LiNbO_3$ and $LiTaO_3$.

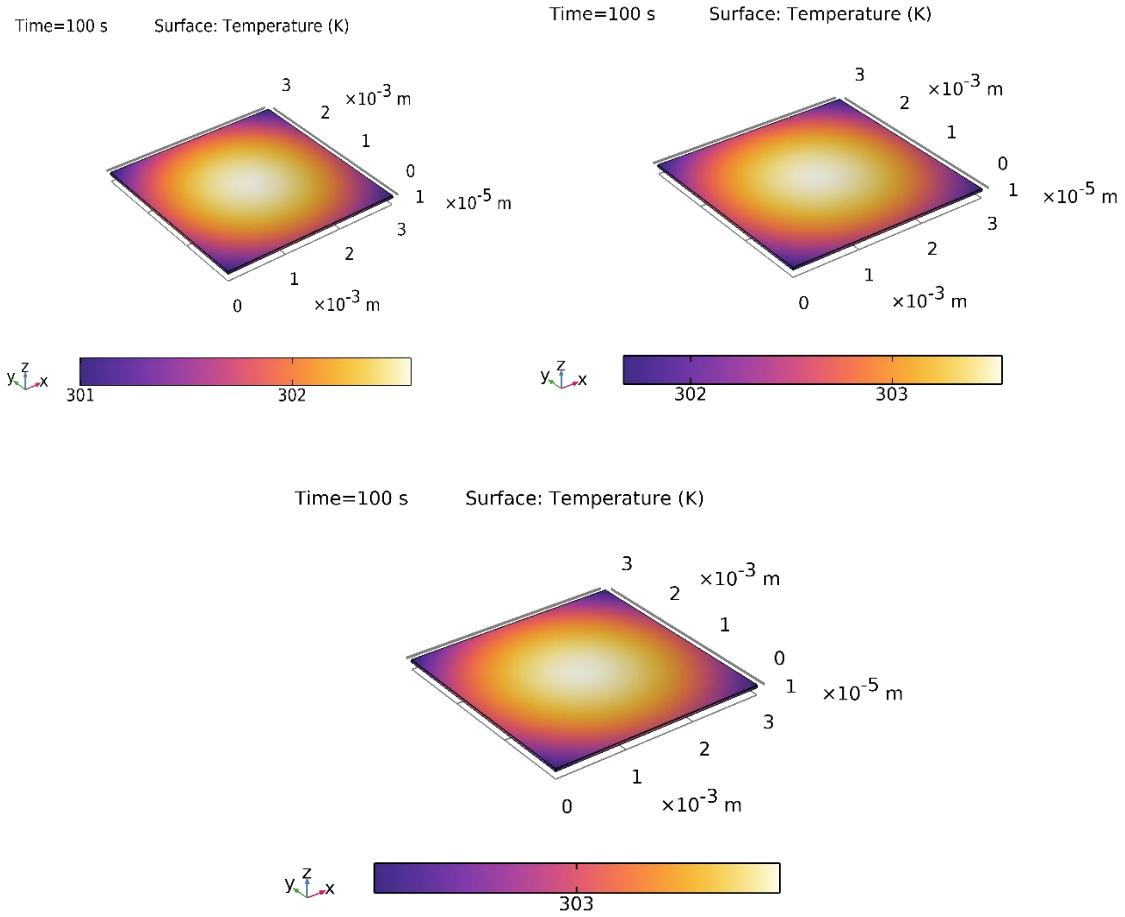

Figure 5: Temperature distribution profile of $LiTaO_3$(top right), $LiNbO_3$ (top left) and AlN (bottom) sensing layer

b. *Isothermal contours (isosurface)*

The isothermal contour profile of a pyroelectric sensing layer plays a crucial role in understanding the temperature distribution and heat flow within the material. When conducting a COMSOL simulation of a pyroelectric sensing layer, the isothermal contour profile shown in figure 6 is obtained by solving the heat transfer equations and considering the boundary conditions, material properties, and heat sources or sinks. The simulation takes into account the thermal conductivity, specific heat, and density of the pyroelectric material. The isothermal contour profile provides a visual representation of the temperature distribution across the sensing layer. The contours are typically displayed in a colour map, where different colours represent different temperature levels. The contours reveal areas of high and low temperatures, allowing for a detailed analysis of the thermal behaviour of the pyroelectric material. It helps in identifying potential hotspots or regions with temperature gradients that could affect the sensor's performance. For $LiTaO_3$, the isothermal contour profile typically shows a temperature range of 301 to 302 K. This range indicates that the majority of the sensing layer remains within this temperature interval during operation. Similarly, for $LiNbO_3$, the isothermal contour profile generally displays a slightly higher temperature range of 302 to 303 K.

This suggests that $LiNbO_3$ has a slightly higher temperature increase compared to $LiTaO_3$ in the sensing layer. Again, the specific temperature distribution is depicted through the contours, allowing for a detailed analysis of the thermal behaviour. In the case of AlN, the isothermal contour profile shows a temperature range of 303 K at the bottom of the sensing layer. This indicates that AlN experiences a slightly greater temperature increase compared to both $LiTaO_3$ and $LiNbO_3$.

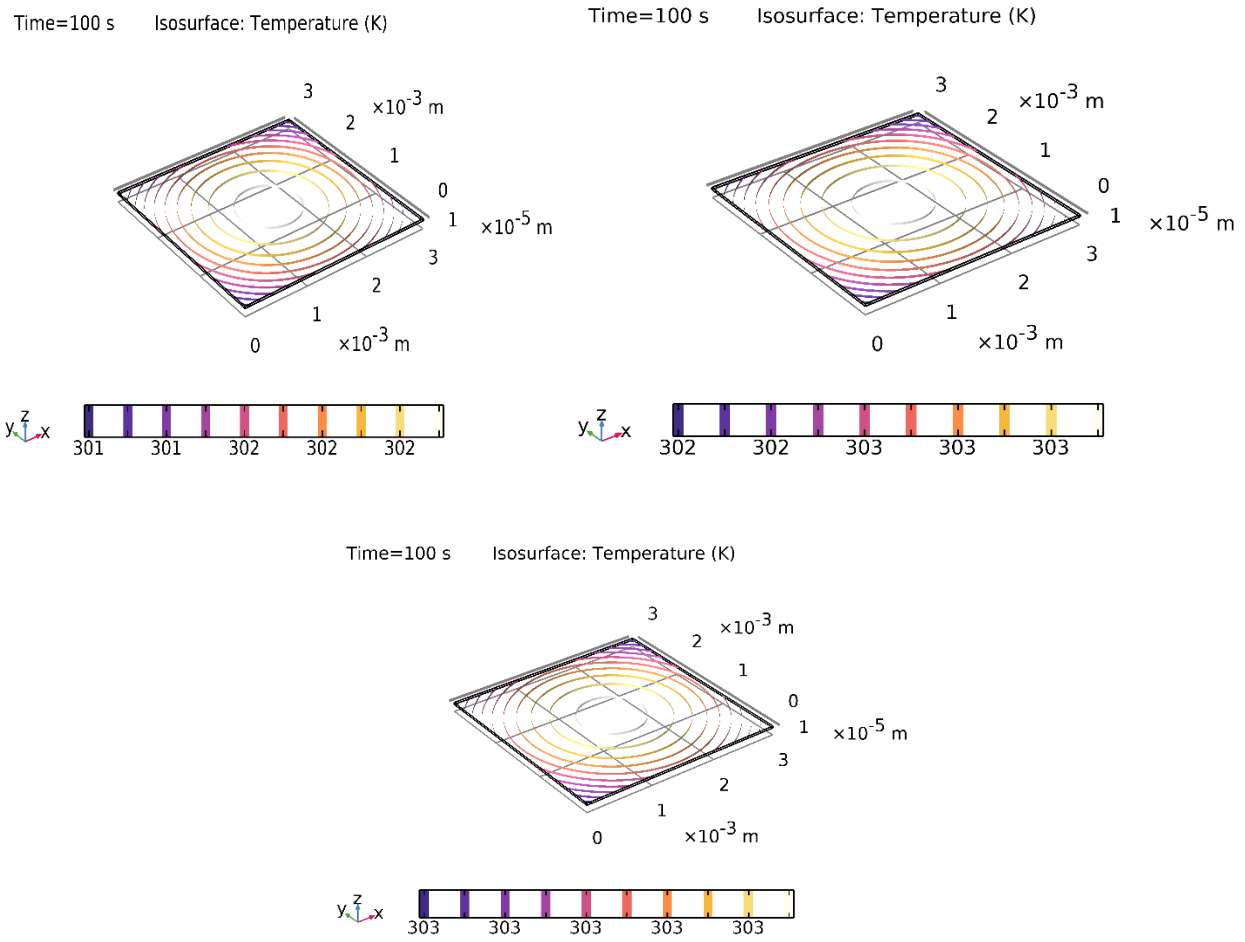

Figure 6: Isothermal contours profile of $LiTaO_3$(top right), $LiNbO_3$ (top left) and AlN (bottom) sensing layer

4.2 Electric analysis of sensing layer

a. Electric potential

The electric potential profile of a pyroelectric sensing layer in COMSOL simulation results represents the distribution of electric potential within the material. In pyroelectric materials, changes in temperature induce electric polarization, resulting in the generation of an electric potential across the sensing layer. When conducting a COMSOL simulation of a pyroelectric sensing layer, the electric potential profile is obtained by solving the electrostatic equations, taking into account the material properties, boundary conditions, and applied electric fields. The simulation considers the pyroelectric coefficients and dielectric properties of the material to accurately capture the electric response. The electric potential value indicates the magnitude of the electric potential at that point in space. Analysing these electric potential values provides valuable insights into the behaviour of the AlN layer as a pyroelectric sensing material. It helps in understanding the electric response and sensitivity of the material to temperature changes. The overall electric potential result of the AlN layer shown in figure 7 is on X-axis coordinate: 0.0015565 volts, Y-axis coordinate: 0.0020701 volts, Z-axis coordinate: 1.5000E-5 volts and

Electric potential value: 2.4377E-6 volts. For the $LiTaO_3$ material, the electric potential distribution within the pyroelectric sensing layer on X-axis coordinate: 0.0015229 volts, Y-axis coordinate: 0.0015203 volts, Z-axis coordinate: 1.5000E-5 volts and Electric potential value: 9.0785E-4 volts. For the $LiNbO_3$ material, the electric potential distribution within the pyroelectric sensing layer is on X-axis coordinate: 0.0014924 volts, Y-axis coordinate: 0.0015000 volts, Z-axis coordinate: 2.2159E-5 volts and Electric potential value: 5.4783E-4 volts. From comparing these values, we have observed some differences in the electric potential distributions among the materials:

- AlN has the highest values in both the x-axis and y-axis coordinates compared to $LiTaO_3$ and $LiNbO_3$. This suggests a relatively higher electric potential across the AlN sensing layer.
- $LiTaO_3$ exhibits slightly lower electric potential values compared to AlN but higher values compared to $LiNbO_3$ in both the x-axis and y-axis coordinates.
- $LiNbO_3$ shows the lowest electric potential values among the three materials, indicating a relatively lower electric potential distribution in the $LiNbO_3$ sensing layer.

These variations in electric potential distributions may arise from differences in material properties, such as the pyroelectric coefficients and dielectric properties of the materials. The specific electric potential distributions provide insights into the behaviour of each material and its sensitivity to temperature changes.

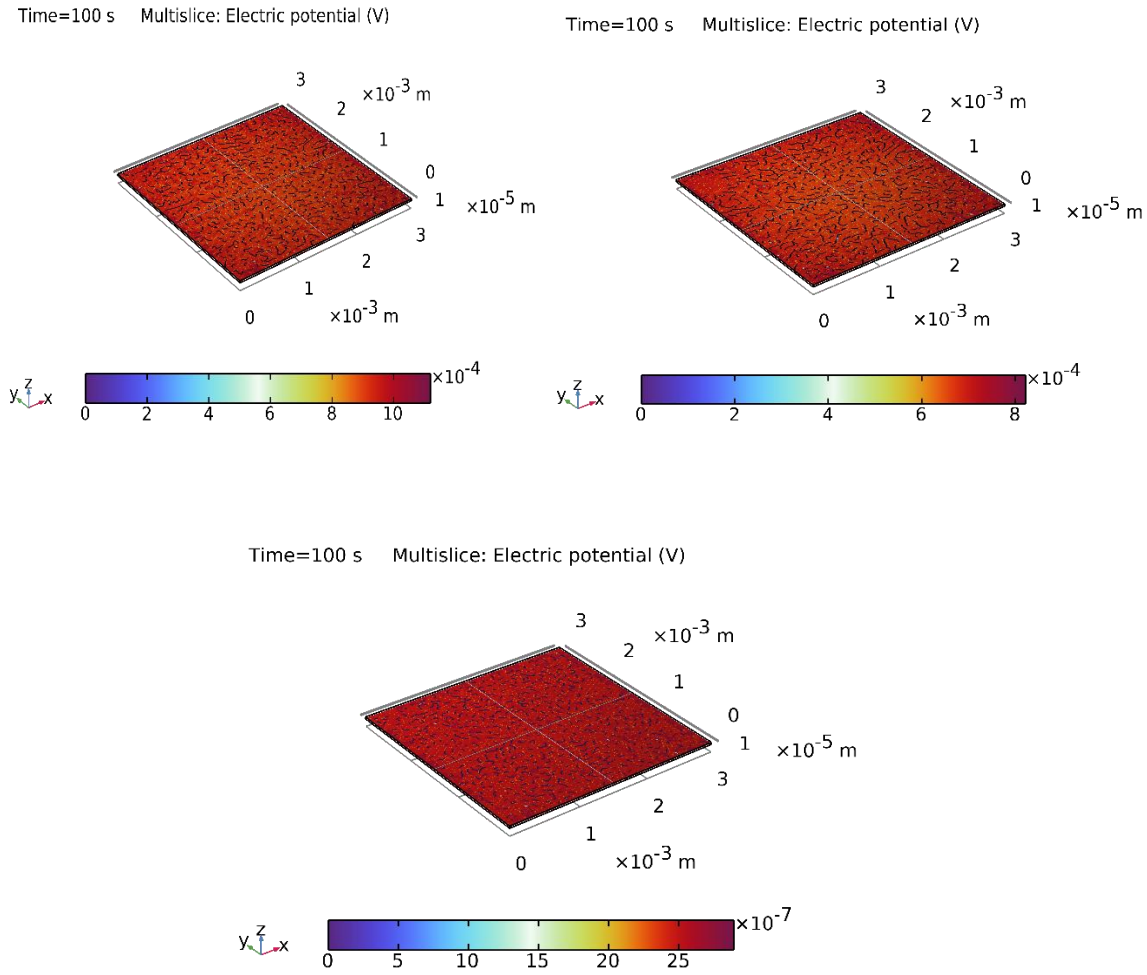

Figure 7: Electric Potential distribution profile of $LiTaO_3$(top right), $LiNbO_3$ (top left) and AlN (bottom) sensing layer

b. Electric field norms

The electric field norms profile of a pyroelectric sensing layer in COMSOL simulation results represents the magnitude of the electric field within the material. In pyroelectric materials, changes in temperature induce electric polarization, resulting in the generation of an electric field across the sensing layer. The electric field norms profile is often visualized graphically, with colors or contour lines representing different magnitudes of the electric field. This visual representation helps in identifying regions with high or low electric field strengths, enabling a detailed analysis of the electric behavior within the sensing layer. The electric field norms profile provides insights into the distribution and intensity of the electric field within the sensing layer. It helps in understanding the sensitivity and performance of the pyroelectric sensor by analyzing the magnitude and spatial distribution of the electric field. Additionally, the electric field norms profile aids in identifying areas of electric field concentration or electric field gradients within the sensing layer. This information is crucial for designing electrode configurations and optimizing the electric field distribution to enhance the sensitivity and performance of the pyroelectric sensor. For the $LiNbO_3$ material, the electric field norm values shown in figure 8 of 0.0015000 volts/meter in the x-axis, 0.0014928 volts/meter in the y-axis, 2.2862E-5 volts/meter in the z-axis, and 51.714 volts/meter as the electric field norms for the $LiNbO_3$ layer provide valuable information for understanding and optimizing the behavior of pyroelectric sensors based on this material. For the $LiTaO_3$ material, the electric field norms values of 0.0014989 volts/meter in the x-axis, 0.0015000 volts/meter in the y-axis, 1.9821E-5 volts/meter in the z-axis, and 43.848 volts/meter as the electric field norms for the LiTaO3 layer provide valuable information for understanding and optimizing the behavior of pyroelectric sensors based on this material. For the AlN material, the electric field norms within the pyroelectric sensing layer is 0.0015317 volts/meter in the x-axis, 0.0015356 volts/meter in the y-axis, 1.5000E-5 volts/meter in the z-axis, and 0.12177 volts/meter as the electric field norms for the AlN layer provide valuable information for understanding and optimizing the behavior of pyroelectric sensors based on this material.

From these values, we can observe some differences in the electric field norms distribution among the materials:

- AlN has significantly lower electric field norm values compared to $LiTaO_3$ and $LiNbO_3$. This suggests a relatively weaker electric field within the AlN sensing layer.
- $LiTaO_3$ exhibits lower electric field norm values compared to $LiNbO_3$, indicating a relatively weaker electric field distribution in the $LiTaO_3$ sensing layer.
- $LiNbO_3$ shows the highest electric field norm values among the three materials, indicating a relatively stronger electric field distribution within the $LiNbO_3$ sensing layer.

These variations in the electric field norms distribution may arise from differences in material properties, such as the pyroelectric coefficients and dielectric properties of the materials. The specific electric field norms provide insights into the intensity and spatial distribution of the electric field within the sensing layer.

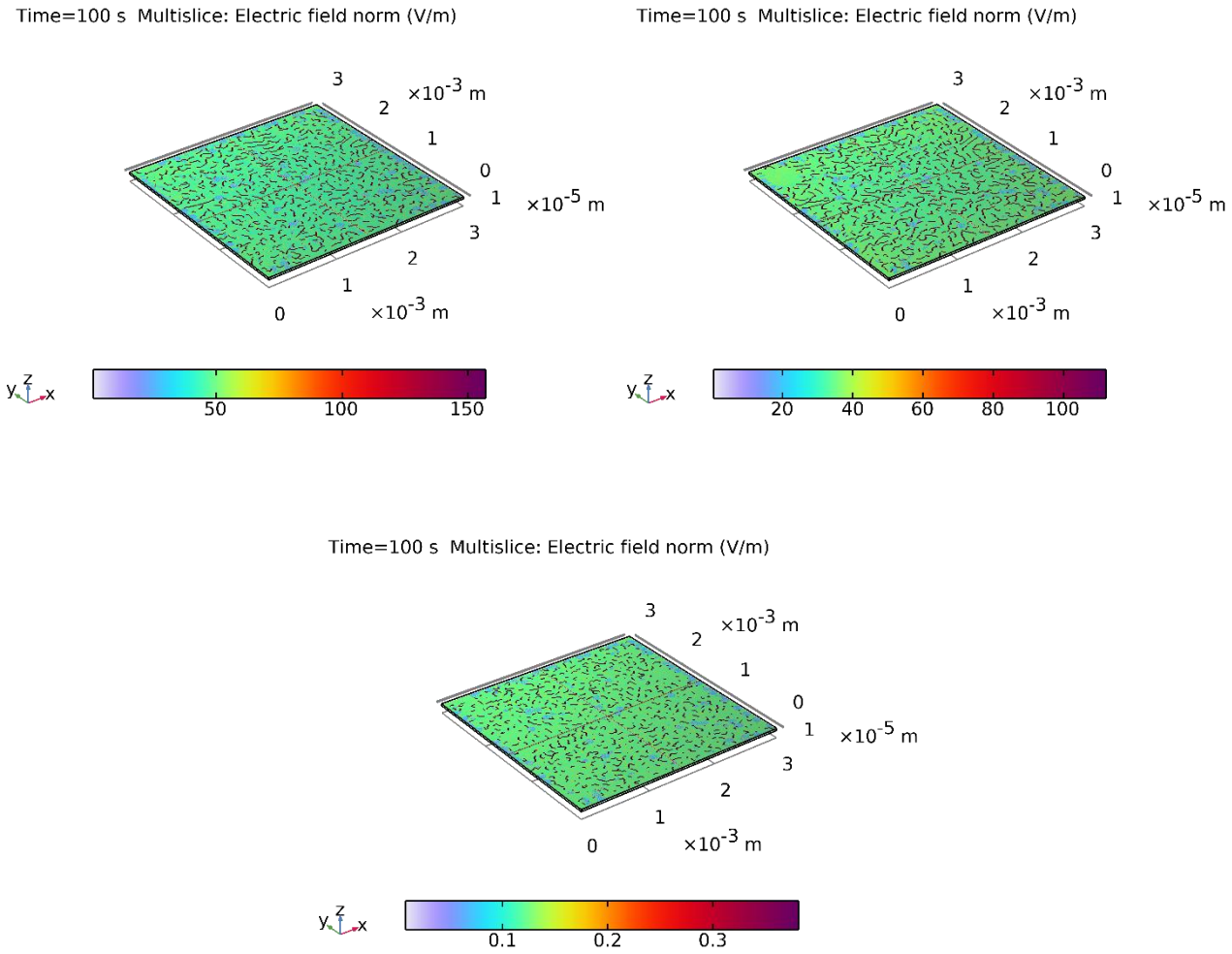

Figure 8: Electric field distribution profile of $LiTaO_3$(top right), $LiNbO_3$ (top left) and AlN (bottom) sensing layer

c. Current through device resistor R

A plot depicting the relationship between temperature and current through resistor R1 over time provides valuable insights into the behaviour of the different sensing materials, namely AlN, $LiTaO_3$, and $LiNbO_3$. Starting with AlN, the plot shown in figure 9 reveals that as time progresses, both the current and temperature exhibit a gradual increase. The current through resistor R1 rises gradually, peaking at approximately 0.35 nanoamperes. This suggests a relatively lower flow of electric charge through the AlN sensing layer compared to the other materials. Concurrently, the temperature measured at the center of the AlN sensing layer experiences a progressive increase, reaching 303 Kelvin. This indicates a gradual buildup of thermal energy within the AlN layer. $LiTaO_3$, the plot demonstrates a similar trend. As time advances, both the current through resistor R1 and the temperature at the center of the $LiTaO_3$ sensing layer increase gradually. The current through R1 reaches a maximum value of approximately 4.8 nanoamperes, indicating a more significant flow of electric charge through the device compared to AlN. The temperature also rises progressively, reaching 301 Kelvin, indicating an escalation in thermal energy within the $LiTaO_3$ layer. In the case of $LiNbO_3$, the plot showcases a comparable pattern. As time elapses, the current through resistor R1 and the temperature at the center of the $LiNbO_3$ sensing layer exhibit a gradual increase. The current through R1 reaches a maximum value of approximately 3.6 nanoamperes, falling between the values observed for AlN and $LiTaO_3$. The temperature rises steadily, reaching

301.5 Kelvin, indicating an augmentation in thermal energy within the $LiNbO_3$ layer. Comparing the maximum currents among the three materials, AlN exhibits the lowest value, $LiTaO_3$ demonstrates the highest, and $LiNbO_3$ falls in between. These variations in current indicate differences in the flow of electric charge and electrical conductivity properties of the respective sensing materials. These findings emphasize the unique electrical characteristics and thermal responses of each material, underscoring the importance of selecting the appropriate sensing material based on the specific requirements and desired performance of the system. In summary, the plot of temperature and current through resistor R1 over time reveals distinct trends for AlN, $LiTaO_3$, and $LiNbO_3$. The variations in current highlight the differences in electrical conductivity and charge flow among the sensing materials, providing valuable insights for optimizing system performance and selecting the most suitable material for specific applications.

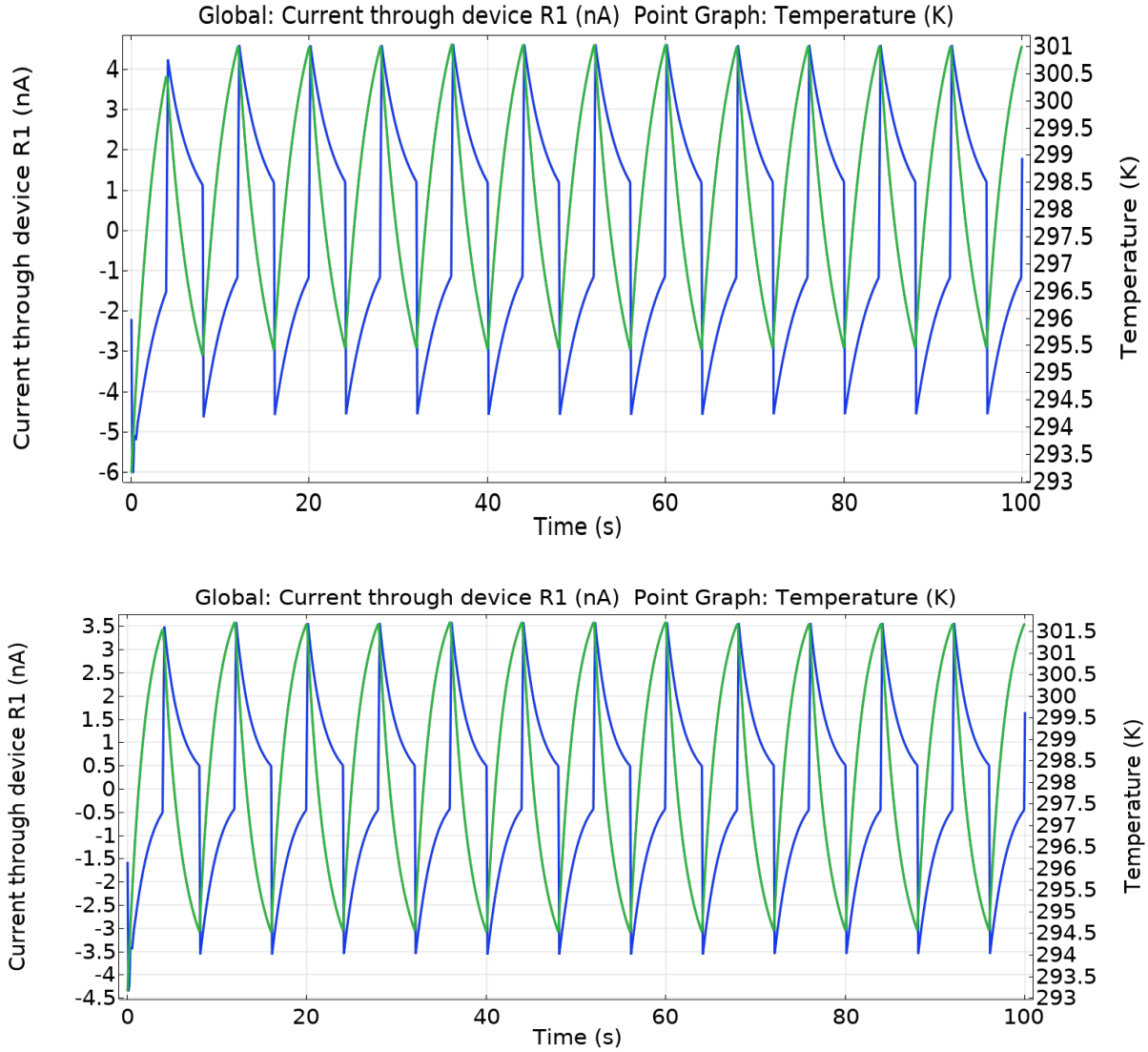

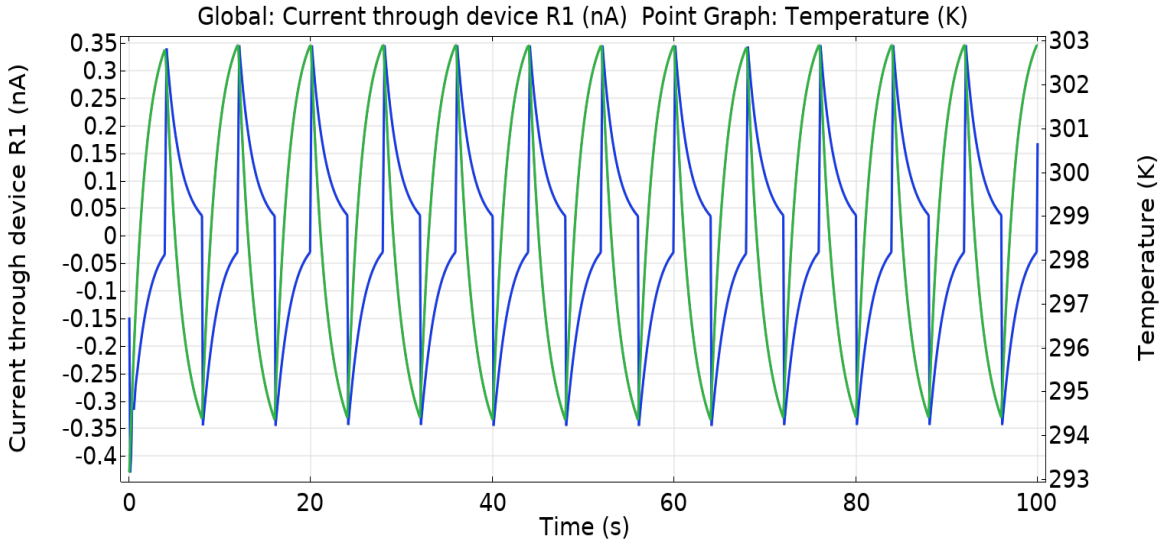

Figure 9: 1D graph of current through device resistor in $LiTaO_3$(top), $LiNbO_3$ (middle) and AlN (bottom) sensing layer

5. Applications

a. Thermal imaging

Thermal imaging of electrical and mechanical systems, low visibility vision system and building systems for preventative measurement could be performed with pyroelectric IR sensors at room temperature. Pyroelectric based IR detector has tremendous potential in applications like crowd control, building management, door counters and evacuation.[26-28]

b. Surveillance

Cameras are conventional security system and process huge data to extract features hence cost is high, whereas IR sensors are low-cost security system.

c. Gas sensors

The pyroelectric-based IR sensors intended to be used in sensing CO_2, CO, SO_2, NO_2 and other poisonous gases, can determine the gas concentration and identify compounds.

d. Night vision

Military transport vehicle like tanks, trucks and personal carriers mostly operates in total darkness hence night vision IR sensors depends on low sky illumination to help the surroundings and targeted scene.

e. Thermal imaging at airports

Thermal imaging system measure the surface skin temperature one of the COVID-19 symptoms. The person who collects the information from the sensors not require any human contact. It is faster and accurate.

f. Motion sensors

IR sensor catch motion of human through the detection of infrared radiated from human body.

6. Future scope

Thermal imaging and IR detections are latest topics of great interest in area like military and commercial ranging from fire-fighting, driving aids, surveillance, night vision, gas sensors and various medical applications. In industrial control, furnace temperature control or in many experiments we need accurate control of the process temperature also temperature is monitored with the help of certain sensors. Pyroelectric infra-red detectors have wide applications in fire alarms, intruder alarms, gas analysis, pollution monitoring, radiometers, pyroelectric thermal imaging and laser detectors. Most recently, there have been huge progress on integrated mid-IR gas sensors, based

on maximum absorption characteristics of gas when interacts with light at certain wavelength for low power, low cost and miniature device. Mid-IR gas sensors used to calculate CO_2 concentration by observing the electrical signal output at certain gas absorption wavelength. The wavelength range of mid- IR for gas sensing is 2µm- 20µm.

7. Conclusions

In conclusion, the simulation results and analysis have provided valuable insights into the behavior of different pyroelectric sensing materials, namely AlN, $LiTaO_3$, and $LiNbO_3$. COMSOL software provides powerful capabilities for studying heat transfer, electrostatics, and Multiphysics phenomena in various applications, such as pyroelectric sensing layers in IR detectors. Its simulation modules allow for accurate analysis, optimization, and design of these systems, considering factors like heat loss, beam orientation, and electric circuit components. AlN demonstrates faster heating (302 K) compared to $LiNbO_3$ (298 K) and $LiTaO_3$ (297 K) in simulated pyroelectric sensing layer temperature distributions. The isothermal contour profiles revealed varying temperature ranges for each material, indicating their sensitivity to thermal changes. The electric potential and electric field norms profiles showcased the distribution and magnitude of the electric potential and field within the sensing layers. The electric potential distributions for AlN (2.4377E-6 V), $LiTaO_3$ (9.0785E-4 V), and $LiNbO_3$ (5.4783E-4 V) in the pyroelectric sensing layer indicate distinct material-specific responses, highlighting variations in electric sensitivity to temperature changes. Furthermore, the comparison of current through resistor R1 highlighted variations among the materials, with $LiTaO_3$ exhibiting the highest current, followed by $LiNbO_3$ and AlN. These findings emphasize the unique electrical and thermal characteristics of each material, providing important information for optimizing system performance and selecting suitable materials for pyroelectric sensing applications. AlN, $LiTaO_3$, and $LiNbO_3$ exhibit distinct trends in maximum current values: AlN (0.35 nA), $LiTaO_3$ (4.8 nA), and $LiNbO_3$ (3.6 nA), reflecting varied electrical conductivity and thermal responses. By leveraging COMSOL's features, researchers and engineers can gain valuable insights into complex phenomena, improving the performance and efficiency of pyroelectric-based devices.

References

[1] Q. L. Tan et al., "The characterization and fabrication of pyroelectric infrared sensors and application of gas monitoring," 2008 2nd IEEE International Nanoelectronics Conference, INEC 2008, vol. 8, pp. 776–781, 2008, doi: 10.1109/INEC.2008.4585599.

[2] Y. Togami, M. Okuyama, Y. Hamakawa, M. Kimata, and M. Denda, "Pyroelectric infrared image sensors using Si CCD and FET arrays," Sensors and Actuators: A. Physical, vol. 40, no. 2, pp. 111–116, 1994, doi: 10.1016/0924-4247(94)85014-3.

[3] R. Takayama, Y. Tomita, J. Asayama, K. Nomura, and H. Ogawa, "Pyroelectric infrared array sensors made of c-axis-oriented La-modified $PbTiO_3$ thin films," Sensors and Actuators: A. Physical, vol. 22, no. 1–3, pp. 508–512, 1990, doi: 10.1016/0924-4247(89)80025-1.

[4] R. Takayama, Y. Tomita, K. Iijima, and I. Ueda, "Pyroelectric properties and application to infrared sensors of $pbti0_3$, $pblati0_3$ and $pbzrti0_3$ ferroelectric thin films," Ferroelectrics, vol. 118, no. 1, pp. 325–342, 1991, doi: 10.1080/00150199108014770.

[5] R. Takayama, Y. Tomita, K. Iijima, and I. Ueda, "Pyroelectric linear array infrared sensors made of c-axis-oriented La-modified $PbTiO_3$ thin films," Journal of Applied Physics, vol. 63, no. 12, pp. 5868–5872, 1988, doi: 10.1063/1.340276.

[6] J. Yun and S. S. Lee, "Human movement detection and identification using pyroelectric infrared sensors," Sensors (Switzerland), vol. 14, no. 5, pp. 8057–8081, 2014, doi: 10.3390/s140508057.

[7] M. Heydarianasl and M. F. ad Rahmat, "Using pyroelectric sensors to detect continuous infrared radiation," Jurnal Teknologi (Sciences and Engineering), vol. 67, no. 3, pp. 51–55, 2014, doi: 10.11113/jt.v67.2764.

[8] T. Liu et al., "Micromachined infrared detectors based on pyroelectric thin films," Eurasip Journal

on Advances in Signal Processing, vol. 2012, no. 1, pp. 0–3, 2012, doi: 10.1016/j.mejo.2008.07.011.
[9] M. Edwards et al., "Characterization of a traffic management system using pyroelectric infrared sensors," TechSym 2011 - Proceedings of the 2011 IEEE Students' Technology Symposium, vol. 8868, no. 3, pp. 319–333, 2013, doi: 10.1088/1742-6596/433/1/012017.
[10] Wang Yuzi, Luo Nengsheng, Liu Wenbin "Micro-scale thermal imaging of organic and polymeric materials with cooled and uncooled infrared cameras," Quantitative InfraRed Thermography Journal, vol. 11, no. 2, pp. 207–221, 2020, doi: 10.3390/MI11090800.
[11] R. Farrell et al., "Pyroelectric Detectors and Materials," Physica Status Solidi (C) Current Topics in Solid State Physics, vol. 66, no. 3–4, pp. 517–520, 2011, doi: 10.1002/pssc.201300513.
[12] C. Ranacher et al., "A cmos compatible pyroelectric mid-infrared detector based on aluminium nitride," Sensors (Switzerland), vol. 19, no. 11, pp. 2–11, 2019, doi: 10.3390/s19112513.
[13] A. Finn, M. Schossig, V. Norkus, and G. Gerlach, "Microstructured surfaces on LiTaO3-based pyroelectric infrared detectors," IEEE Sensors Journal, vol. 11, no. 10, pp. 2204–2211, 2011, doi: 10.1109/JSEN.2011.2128307.
[14] Y. Querner, V. Norkus, and G. Gerlach, "The use of thermal effects for increasing the responsivity of pyroelectric detectors," Proceedings of IEEE Sensors, pp. 853–856, 2011, doi: 10.1109/ICSENS.2011.6127218.
[15] T. Ott, M. Schossig, V. Norkus, and G. Gerlach, "Efficient thermal infrared emitter with high radiant power," Journal of Sensors and Sensor Systems, vol. 4, no. 2, pp. 313–319, 2015, doi: 10.5194/jsss-4-313-2015.
[16] V. Norkus, M. Schossig, G. Gerlach, and R. Köhler, "New pyroelectric detectors for pyrometry and security technique," International Conference on Solid-State and Integrated Circuits Technology Proceedings, ICSICT, pp. 2379–2382, 2008, doi: 10.1109/ICSICT.2008.4735071.
[17] V. Norkus, R. Koehler, and G. Gerlach, "Pyroelectric single-element detectors for special applications," Infrared Technology and Applications XXX, vol. 5406, no. 1, p. 836, 2004, doi: 10.1117/12.542047.
[18] V. Norkus, A. Schulze, Y. Querner, and G. Gerlach, "Thermal effects to enhance the responsivity of pyroelectric infrared detectors," Procedia Engineering, vol. 5, no. February, pp. 944–947, 2010, doi: 10.1016/j.proeng.2010.09.264.
[19] M. Schossig, V. Norkus, and G. Gerlach, "Infrared responsivity of pyroelectric detectors with nanostructured NiCr thin-film absorber," IEEE Sensors Journal, vol. 10, no. 10, pp. 1564–1565, 2010, doi: 10.1109/JSEN.2010.2046162.
[20] D. K. T. Ng et al., "Considerations For an 8-inch Wafer-Level CMOS Compatible AlN Pyroelectric 5-14 μm Wavelength IR Detector Towards Miniature Integrated Photonics Gas Sensors," Journal of Microelectromechanical Systems, pp. 1–9, 2020, doi: 10.1109/jmems.2020.3015378.
[21] I. Shibasaki and N. Kuze, Mass Production of Sensors Grown by Molecular Beam Epitaxy, no. 1960. Elsevier Inc., 2018.
[22] Y. Jing et al., "Design and optimization of an integrated MEMS gas chamber with high transmissivity," Digital Communications and Networks, no. May, 2020, doi: 10.1016/j.dcan.2020.05.006.
[23] V. Norkus, G. Gerlach, and R. Köhler, "A new chip layout for pyroelectric single-element detectors with high D* and very low microphonics," Infrared Technology and Applications XXXV, vol. 7298, p. 72982D, 2009, doi: 10.1117/12.819449.
[24] V. Norkus et al., "Thermal effects to enhance the responsivity of pyroelectric infrared detectors," Procedia Engineering, vol. 5, no. February, pp. 944–947, 2010, doi: 10.1016/j.proeng.2010.09.264.
[25] R. Lehmkau, M. Ebemann, D. Mutschall, N. Neumann, J. Lienig, and I. Gmbh, "Thermal-electrical Design Improvements of a New CMOS Compatible Pyroelectric Infrared Sensor Based on HfO 2," pp. 143–144, 2020, doi: 10.5162/SMSI2020/C1.1.
[26] Saurabh, Nishchay, et al. "Solar Energy Harvesting Using Lead-Free Pyroelectric Bulk Ceramics: A Simulation Study." Journal of Science: Advanced Materials and Devices, vol. 8, no. 1, Mar. 2023, p. 100527, https://doi.org/10.1016/j.jsamd.2022.100527. Accessed 11 Dec. 2023.
[27] Boiko, Andrei, et al. "Contactless Technologies, Sensors, and Systems for Cardiac and Respiratory

Measurement during Sleep: A Systematic Review." Sensors, vol. 23, no. 11, 24 May 2023, p. 5038, https://doi.org/10.3390/s23115038. Accessed 11 Dec. 2023.
[28] WANG, Yuying, et al. "State-of-The-Art Development about Cryogenic Technologies to Support Space-Based Infrared Detection." Chinese Journal of Aeronautics, vol. 36, no. 12, Dec. 2023, pp. 32–52, https://doi.org/10.1016/j.cja.2023.08.008. Accessed 11 Dec. 2023.